FBXL5 depletion as a novel strategy against osteosarcoma: Evidence for MEK/ERK inhibition and enhanced therapeutic sensitivity

YAN-CHAO MA[1*], WEN-MING ZHOU[1,2*], YONG-QIANG SHI[1,2], YAN-BO DONG[1,2], HAI-HONG ZHANG[1] and WEI NAN[1,2]

[1]Department of Orthopedics, The Second Hospital and Clinical Medical School, Lanzhou University, Lanzhou, Gansu 730000, P.R. China; [2]Orthopedics Key Laboratory of Gansu Province, The Second Hospital of Lanzhou University, Lanzhou, Gansu 730000, P.R. China

Received August 7, 2025; Accepted May 7, 2026

DOI: 10.3892/ol.2026.15726

Abstract. Osteosarcoma (OS) is the most common primary malignant bone tumor in adolescents. Despite standard treatments, including surgery and chemotherapy, the 5-year survival rate for metastatic OS remains <20%, underscoring the need for novel therapeutic targets. F-box and leucine-rich repeat protein 5 (FBXL5) is an E3 ubiquitin ligase that regulates iron homeostasis and exhibits complex functions across different tumors; however, its role in OS is still unclear. The present study employed the MG63 and 143B OS cell lines to investigate the oncogenic potential of FBXL5 through *in vitro* and *in vivo* experiments. Lentivirus-mediated FBXL5 knockdown significantly suppressed cell proliferation, migration and invasion, while promoting apoptosis. RNA sequencing analysis after FBXL5 silencing revealed significant alterations in the mitogen-activated protein kinase signaling pathway, particularly affecting the mitogen-activated protein kinase (MEK)/extracellular signal-regulated kinase (ERK) axis. Consequently, FBXL5 depletion reduced the expression and phosphorylation of Ras, Raf, MEK and ERK. In a mouse xenograft tumor model, FBXL5 knockdown inhibited tumor growth and reduced tumor volume. These findings suggest that FBXL5 promotes OS progression via regulation of the MEK/ERK signaling pathway, suggesting that it may be a useful therapeutic target and potential prognostic indicator; further validation in larger clinical cohorts is warranted.

Correspondence to: Professor Hai-Hong Zhang or Professor Wei Nan, Department of Orthopedics, The Second Hospital and Clinical Medical School, Lanzhou University, 82 Cuiying Men Road, Chengguan, Lanzhou, Gansu 730000, P.R. China
E-mail: zhanghh22@foxmail.com
E-mail: nwei2023@163.com

*Contributed equally

Key words: osteosarcoma, F-box and leucine-rich repeat protein 5, E3 ubiquitin ligase, mitogen-activated protein kinase kinase/extracellular signal-regulated kinase signaling pathway, apoptosis

Introduction

Osteosarcoma (OS) is a common primary malignant bone tumor predominantly affecting adolescents and young adults. A population-based study using the Surveillance, Epidemiology, and End Results (SEER) database reported that the 5-year survival rate for patients with metastatic OS ranges from 10 to 30% (1). Despite advancements in multimodal therapy for patients with localized OS, treatment outcomes for patients with metastatic or recurrent disease remain limited, with 5-year survival rates ranging from 10-30% (2,3). OS is highly metastatic, especially to the lungs (4), and is characterized by resistance to conventional chemotherapy, with the underlying mechanisms remaining complex and poorly understood (5,6). Although genomic studies have revealed alterations in tumor suppressor genes, such as tumor protein 53 and retinoblastoma 1, existing targeted therapies have not effectively addressed the challenges in OS treatment (6,7). This suggests that, in addition to classical genetic mutations, mechanisms such as post-translational modifications, epigenetic regulation and protein degradation serves critical roles in the onset and progression of OS, highlighting the need for further research to uncover novel therapeutic targets.

The E3 ubiquitin ligase family is a core component of the ubiquitin-proteasome system, serving crucial roles in regulating protein stability, the cell cycle, signal transduction and other processes. F-box and leucine-rich repeat protein 5 (FBXL5), a member of the Skp1-Cullin-F-box protein complex, has been recognized as an important sensor of oxygen and iron homeostasis, participating in the regulation of cellular iron homeostasis by controlling the degradation of iron regulatory protein 2 (IRP2) (8,9). FBXL5 not only serves a pivotal role in iron metabolism but also mediates the ubiquitin-mediated degradation of various substrates, thereby regulating cellular processes such as cell cycle progression, DNA damage response and apoptosis (10). These distinct functions position FBXL5 as a potential regulatory factor with significant roles in multiple biological processes.

Although the role of FBXL5 in various tumors has been preliminarily investigated, to the best of our knowledge, its specific function in OS remains underexplored. Studies have demonstrated that FBXL5 exerts different roles in various types of malignant tumors. For example, in gastric cancer, FBXL5 inhibits the epithelial-mesenchymal transition (EMT) and tumor metastasis through the ubiquitin-mediated degradation of the transcription factor Snail1 (11). By contrast, in hepatocellular carcinoma (12,13) and clear cell renal cell carcinoma (ccRCC), the reduced expression of FBXL5 is associated with a poor prognosis, suggesting that FBXL5 may function as a tumor suppressor in these cancers. However, the role of FBXL5 in OS has not been extensively examined.

The mitogen-activated protein kinase (MAPK)/extracellular signal-regulated kinase (ERK) signaling pathway is a critical regulator of fundamental cellular processes such as proliferation, migration, differentiation and apoptosis (14), and serves a pivotal role in the initiation and progression of various malignant tumors. Activation of this pathway is mediated through a cascade of signaling molecules, including Ras, Raf, MAPKK (MEK) and ERK, ultimately regulating the activity of downstream transcription factors and protein kinases to promote tumor cell proliferation and migration (15). In OS, aberrant activation of the MAPK/ERK signaling pathway is closely linked to tumor metastasis and resistance (16,17). Therefore, investigating the upstream regulatory mechanisms of this pathway is crucial for understanding the progression of OS.

The present study investigated the potential role of FBXL5 in the progression of OS. Using RNA sequencing (RNA-seq), we analyzed the impact of FBXL5 knockdown on the transcriptome of OS cells. Therefore, the aim of the present study was to investigate the role of FBXL5 in OS and its potential interaction with the MAPK/ERK signaling pathway. To address this aim, the present study examined the effect of FBXL5 depletion on the expression of MAPK/ERK pathway-related genes, as well as on OS cell proliferation, apoptosis, migration and invasion. These findings highlight the need to identify novel therapeutic targets and understand their clinical relevance.

Materials and methods

Clinical samples. The present study collected tumor and paired normal bone tissues from 6 patients with OS at The Second Hospital of Lanzhou University (Lanzhou, China) between October 2021 and December 2023. The cohort consisted of 6 patients (5 men; 1 woman), aged 14-21 years, with pathological diagnoses of conventional OS (n=5) and parosteal OS (n=1). The inclusion criteria were: i) Histopathologically confirmed diagnosis of conventional or parosteal OS; ii) aged between 10 and 25 years; iii) no prior neoadjuvant chemotherapy or radiotherapy before surgery; iv) availability of both tumor and paired normal bone tissue. The exclusion criteria were: i) Recurrent or metastatic OS at diagnosis; ii) history of other malignancies; iii) insufficient tissue quality or quantity for downstream analysis. All samples were immediately frozen in liquid nitrogen after surgery and stored at -80˚C. The study was approved by The Second Hospital of Lanzhou University ethics committee (approval no. 2024A-504), and written informed consent was obtained from all patients or their guardians.

Cell culture and reagents. The human OS cell lines MG63 and 143B, along with the normal osteoblast cell line hFOB1.19, were purchased from Shanghai Yilei information Technology Co., Ltd. The cells were cultured in high-glucose Dulbecco's Modified Eagle's Medium (HyClone™; Cytiva) supplemented with 10% fetal bovine serum (Gibco; Thermo Fisher Scientific, Inc.). MG63 and 143B cells were incubated at 37˚C, whereas hFOB1.19 cells were maintained at 34˚C.

Lentivirus-mediated gene knockdown. FBXL5-targeting short hairpin RNA (shRNA) lentiviral constructs (cat. no. GXDL0418586; FBXL5 Human GV493) were obtained from Shanghai GeneChem Co., Ltd. The target sequences were as follows: FBXL5-RNAi (118431-1): GTACAGGAA CAGCTTTAAGAA; FBXL5-RNAi (118432-1): CCTGAT GATGAATGGGTGAAA; FBXL5-RNAi (118433-1): GCA CTTTACTCATAGCACATT. A second-generation lentiviral packaging system was used, including the shuttle vector GV493 (hU6-MCS-CBh-gcGFP-IRES-puromycin) and packaging plasmids psPAX2 and pMD2.G. Lentiviral particles were produced in 293T cells (Shanghai GeneChem Co., Ltd.) according to the manufacturer's protocol. Plasmids were transfected at a ratio of 20 (GV493), 15 (psPAX2) and 10 μg (pMD2.G), followed by incubation at 37˚C with 5% CO_2 for 48 h. Viral supernatants were collected and concentrated by ultracentrifugation (13,680 x g; 2 h; 4˚C). For transduction, 143B and MG63 cells were infected with lentivirus at multiplicities of infection (MOI) of 15 and 30, respectively, in the presence of polybrene (8 μg/ml). After 48 h, stable clones were selected using puromycin (2 μg/ml), and selection was maintained for 7 days to establish stable knockdown pools. Knockdown efficiency was confirmed by western blotting (WB) analysis and reverse transcription-quantitative PCR (RT-qPCR). All subsequent experiments were performed 10 days after the initial transduction.

RNA extraction and RT-qPCR. Total RNA was extracted from cells using Trizol (total RNA extraction reagent; cat. no. R0016; Beyotime Biotechnology). RT was performed using the Evo M-MLV One-step RT-PCR kit (with gDNA removal, for qPCR; cat. no. AG11705; AGbio) according to the manufacturer's protocol. The reaction conditions for RT were: 37˚C for 15 min (gDNA removal), 42˚C for 15 min (RT), followed by 85˚C for 5 sec (enzyme inactivation). For qPCR, the reaction was performed using SYBR Green Master Mix (cat. no. AG11732; AGbio), which contains SYBR Green as the fluorophore. The following thermocycling conditions were applied: initial denaturation at 95˚C for 30 sec, followed by 40 cycles of 95˚C for 5 sec and 60˚C for 30 sec. GAPDH was used as the reference gene. The primer sequences used are provided in Table I. Relative expression levels were calculated using the $2^{-\Delta\Delta Cq}$ method (18).

Protein extraction and western blot analysis. Total proteins were extracted from cells using RIPA lysis buffer (cat. no. P0013B; Beyotime Biotechnology) and quantified by the BCA method. Proteins (30 μg/lane) were separated by

Table I. Primer sequences used in the quantitative PCR experiment.

Primer	Primer sequence (5'-3')
FBXL5 forward	TTGTCCTAACCTGGAGCATCTGG
FBXL5 reverse	GCAACCAAGCCAAGACCAACTG
GAPDH forward	AGGTGAAGGTCGGAGTCAACG
GAPDH reverse	GCTCCTGGAAGATGGTGATGG

10% SDS-PAGE and electrotransferred to a PVDF membrane (MilliporeSigma). After blocking with 5% non-fat milk (cat. no. MA0406; Dalian Meilun Biology Technology Co., Ltd.cat. no.) at 4˚C for 1 h, the membrane was incubated with primary antibodies at 4˚C overnight. The primary antibodies and their cat. nos. were as follows: FBXL5 (1:1,000; cat. no. BD-PT6983; Biodragon Immunotechnologies Co., Ltd.), PCNA (1:2,000; cat. no. 10205-2-AP; Proteintech Group, Inc.), CDK4 (1:1,000; cat. no. 11026-1-AP Proteintech Group, Inc.), cyclin D1 (1:1,000; cat. no. 60186-1-Ig; Proteintech Group, Inc.), Bcl-2 (1:1,000; cat. no. AF6139; Affinity Biosciences, Ltd.), Bax (1:1,000; cat. no. AF0120; Affinity Biosciences, Ltd.), cleaved caspase-3 (1:1,000; cat. no. AF7022; Affinity Biosciences, Ltd.), total caspase-3 (1:1,000; cat. no. db12058; Hangzhou Diagbio Technology Co., Ltd.), MMP2 (1:1,000; cat. no. RM8377; Biodragon Immunotechnologies Co., Ltd.), MMP9 (1:1,000; cat. no. RM3763; Biodragon Immunotechnologies Co., Ltd.), MEK1/2 (1:1,000; HUABIO; cat. no. ET1602-3), ERK (1:1,000; cat. no. ET1601-29; HUABIO), Ras (1:1,000; cat. no. RM7373; Biodragon Immunotechnologies Co., Ltd.), Raf (1:1,000; cat. no. RM4242; Biodragon Immunotechnologies Co., Ltd.), and β-actin (1:8,000; cat. no. HA722023; HUABIO). After washing, the membrane was incubated with horseradish peroxidase-conjugated goat anti-rabbit/mouse IgG (1:10,000; cat. no. ZB-2306; Beijing Zhongshan Jinqiao Biotechnology Co., Ltd.) at 4˚C for 1 h. Proteins were detected using enhanced chemiluminescence substrate (cat. no. G2020-500ML; Wuhan Servicebio Technology Co., Ltd.). Densitometric analysis was performed using ImageJ software (version 1.52a; National Institutes of Health).

Immunofluorescence. 143B and MG63 cells were seeded on coverslips, fixed with 4% paraformaldehyde in PBS at room temperature for 15 min, permeabilized with 0.1% Triton X-100 in PBS for 10 min at room temperature and blocked with 5% normal goat serum (cat. no. SL038; Beijing Solarbio Science & Technology Co., Ltd.) in PBS at room temperature for 1 h. After blocking, cells were incubated overnight at 4˚C with the following primary antibodies: FBXL5 (1:100; Santa Cruz Biotechnology, Inc.; cat. no. sc-390102), PCNA (1:100; cat. no. 10205-2-AP; Proteintech Group, Inc.cat. no.), CDK4 (1:100; cat. no. 11026-1-AP; Proteintech Group, Inc.), and cyclin D1 (1:100; cat. no. 60186-1-Ig; Proteintech Group, Inc.cat. no.). After washing, cells were incubated with Alexa Fluor 488-conjugated secondary antibody (1:200; Biodragon Immunotechnologies Co., Ltd.; cat. no. BD9010) at room temperature for 1 h. Nuclei were counterstained with DAPI (1 μg/ml) at room temperature for 5 min. Fluorescence images were captured using a fluorescence microscope.

Functional assays. Proliferation: Cell viability was assessed using the Cell Counting Kit-8 (CCK-8) assay (cat. no. C0038; Beyotime Biotechnology). Cells were seeded in 96-well plates and cultured for 24, 48 and 72 h. At each time point, CCK-8 reagent was added and incubated for 2 h at 37˚C, and the absorbance was measured at 450 nm using a microplate reader. Proliferation rates were also determined using 5-ethynyl-2'-deoxyuridine (EdU) staining with the EdU-488 Cell Proliferation Kit (cat. no. C0071S; Beyotime Biotechnology) according to the manufacturer's instructions. Briefly, cells were incubated with EdU at 37˚C for 2 h, then fixed with 4% paraformaldehyde in PBS at room temperature for 15 min, permeabilized with 0.3% Triton X-100 in PBS and stained with the Click-It reaction mixture. Nuclei were counterstained with DAPI (cat. no. C1006; Beyotime Biotechnology). Images were captured using a fluorescence microscope.

Apoptosis: Apoptotic cells were identified using the TUNEL staining. Cells were fixed with 4% paraformaldehyde in PBS at room temperature for 15 min, permeabilized with 0.1% Triton X-100 in PBS for 5 min and then incubated with TUNEL reaction mixture (cat. no. C1088; Beyotime Biotechnology) at 37˚C for 60 min according to the manufacturer's protocol. Nuclei were counterstained with DAPI (1 μg/ml) at room temperature for 5 min. After rinsing with PBS, the slides were mounted using anti-fade mounting medium (Beyotime Biotechnology China; cat. no. P0126). At least five random fields of view per sample were observed under a fluorescence microscope, and TUNEL-positive cells were counted.

Migration: A wound healing assay was performed to measure cell migration. No substrate coating was used. 143B and MG63 cells were seeded in 6-well plates and cultured until reaching 90-100% confluence. A linear scratch was created across the cell monolayer using a sterile 200 μl pipette tip. Debris was removed by washing with PBS, and cells were then cultured in Gibco (Thermo Fisher Scientific, Inc.) basal medium to exclude the effect of proliferation. Wound closure was monitored and imaged at 0, 24, 48, 72 and 96 h under a light microscope. The wound area was measured using ImageJ software (version 1.52a, National Institutes of Health), and the percentage of wound closure was calculated as: [(area at 0 h-area at time point)/area at 0 h] x100%. No drugs were used in this assay.

Animal experiment. A total of 36 BALB/c nude mice (4-6 weeks old; female; weighing 16-18 g) were obtained from Lanzhou Veterinary Research Institute, Chinese Academy of Agricultural Sciences. Mice were housed under specific pathogen-free conditions with temperature 22±2˚C, humidity 50±10%, a 12 h light/dark cycle, and ad libitum access to food and water. Mice were randomly assigned to six groups (n=6 per group): Group 1: 143B + control; group 2: 143B + sh-NC; group 3: 143B + sh-FBXL5; group 4: MG63 + control; group 5: MG63 + sh-NC; group 6: MG63 + sh-FBXL5. A xenograft tumor model was established by subcutaneously injecting $2x10^6$ cells into the right axilla of each mouse. Tumor volume was measured every 3 days using a caliper and calculated as volume=(length x width^2)/2. The ethical endpoint was defined

as tumor volume >1,500 mm^3, tumor ulceration, substantial weight loss (>20% of initial body weight) or signs of pain/distress. Tumor volume and body weight were measured every 3 days from day 0 until the endpoint for each group. The 143B xenografts grew more rapidly and reached the ethical endpoint (tumor volume >1,500 mm^3) by day 30, whereas the MG63 xenografts grew more slowly and did not reach the endpoint until day 34. Therefore, mice in the 143B and MG63 groups were euthanized on day 30 and day 34, respectively, to prevent exceeding the predefined ethical endpoints. No mice were euthanized before the scheduled endpoints. Mice in the 143B and MG63 groups were euthanized by CO_2 inhalation (30-50% vol/min) on day 30 and day 34, respectively. The tumor tissues were then processed for subsequent analysis. The animal study was approved by the Animal Ethics Committee of Lanzhou University Second Hospital (approval no. D2024-417).

RNA-seq. Total RNA was extracted from cells using TRIzol reagent (cat. no. R0016; Beyotime Biotechnology). RNA integrity was assessed using an Agilent 2100 Bioanalyzer (Agilent Technologies, USA). Sequencing libraries were prepared using the TruSeq RNA Sample Prep Kit v2 (Illumina, Inc.; cat. no. RS-122-2001) according to the manufacturer's protocol. The libraries were sequenced on the Illumina NovaSeq 6000 platform (Illumina, Inc.) using the NovaSeq 6000 S4 Reagent Kit v1.5 (300 cycles; Illumina, Inc.; cat. no. 20028312) with 150 bp paired-end sequencing. The final library was loaded at a concentration of 1.8 pM, as measured by Qubit 2.0 Fluorometer (Thermo Fisher Scientific, Inc.). For data analysis, Trimmomatic (version 0.39; http://www.usadellab.org/cms/index.php?page=trimmomatic) was used for quality control, HISAT2 (version 2.2.1; http://ccb.jhu.edu/software/hisat2/) was used for alignment to the reference genome, and featureCounts (version 2.0.1; http://subread.sourceforge.net/) was used to quantify gene expression levels. edgeR (version 3.40.0) was applied to identify differentially expressed genes (DEGs) with criteria of $|\log_2 FC| \geq 1$ and FDR ≤ 0.05. Functional enrichment analysis was conducted using GOATools (version 1.0.0; https://github.com/tanghaibao/GOatools) for Gene Ontology (GO) enrichment and KOBAS (version 3.0; http://bioinfo.org/kobas3/) for KEGG pathway enrichment. DAVID (Database for Annotation, Visualization and Integrated Discovery; https://david.ncifcrf.gov) and GSEA (Gene Set Enrichment Analysis; http://www.gsea-msigdb.org/gsea/index.jsp) were also used for functional annotation and enrichment analysis.

Immunofluorescence (IF). After deparaffinization in xylene and rehydration through a graded ethanol series, antigen retrieval was performed by heating the paraffin-embedded tissue sections in citrate buffer (pH 6.0) at 95˚C for 15 min. Sections were incubated with primary antibodies against Raf (1:100; cat. no. RM4242; Suzhou Botron Immunotherapy Technology Co., Ltd.) and MEK1/2 (1:100; HUABIO; cat. no. ET1602-3) at 4˚C overnight. After washing, sections were incubated with Alexa Fluor 488-conjugated secondary antibody (1:200; Biodragon Immunotechnologies Co., Ltd.; cat. no. BD9010) at room temperature for 1 h. Nuclei were counterstained with DAPI (1 μg/ml) at room temperature for 10 min. Fluorescence images were captured using a fluorescence microscope.

H&E staining. Paraffin-embedded tissue sections were deparaffinized in xylene and rehydrated through a graded ethanol series (100, 95, 70 and 50%) for 2 min each, followed by rinsing in distilled water. Sections were stained with hematoxylin at room temperature for 5 min, followed by eosin staining at room temperature for 2 min. Sections were then dehydrated through a graded ethanol series (70, 95 and 100%), cleared in xylene, and mounted with a coverslip using a resinous mounting medium. Images were captured using a light microscope (Olympus Corporation) and analyzed using ImageJ software (version 1.52a; National Institutes of Health).

Statistical analysis. All experimental data were statistically analyzed using GraphPad Prism 8.0.2 software (GraphPad; Dotmatics). A paired Student's t-test was used when comparing two measurements from the same subject, whereas an unpaired Student's t-test was used when comparing data from different groups of subjects. For multiple groups, one-way ANOVA was used, followed by Tukey's multiple comparisons test. Data are expressed as the mean ± standard deviation from six independent repeats. Fluorescence images and WB bands were analyzed and measured using ImageJ 1.52a software (National Institutes of Health). $P<0.05$ was considered to indicate a statistically significant difference.

Results

FBXL5 expression in OS tissues and cells is significantly higher compared with normal controls, and a FBXL5 knockdown model was successfully established in 143B and MG63 cells. qPCR and WB analyses revealed that FBXL5 protein (Fig. 1A) and mRNA (Fig. 1B) expression levels were significantly elevated in OS tissues compared to normal tissues. In OS cell lines 143B and MG63, FBXL5 mRNA (Fig. 1D and F) and protein (Fig. 1C and E) expression was also significantly upregulated compared with the normal osteoblast cell line hFOB1.19.

Lentivirus-mediated RNA interference successfully established stable FBXL5 knockdown cell lines, with infection rates exceeding 99% in 143B (Fig. 1G) and MG63 (Fig. 1L) cells. qPCR results showed significantly lower FBXL5 mRNA levels in the sh-FBXL5 group compared with the control and NC groups in both 143B (Fig. 1H) and MG63 (Fig. 1M) cells. WB analysis further confirmed a marked reduction in FBXL5 protein expression in the sh-FBXL5-1 group of 143B (Fig. 1I and J) and MG63 (Fig. 1N and O) cells compared with the control group. Immunofluorescence analysis also demonstrated significantly decreased FBXL5 expression in the sh-FBXL5-1 group in both 143B (Fig. 1K) and MG63 (Fig. 1P) cells compared with the control and NC groups.

These results demonstrate that FBXL5 is highly expressed in OS tissues and cell lines, providing experimental support for investigating its functional role in OS. Lentivirus-mediated RNA interference successfully knocked down FBXL5 expression, with the sh-FBXL5-1 sequence reducing both mRNA and protein expression levels. Therefore, subsequent experiments were conducted using the sh-FBXL5-1 lentivirus.

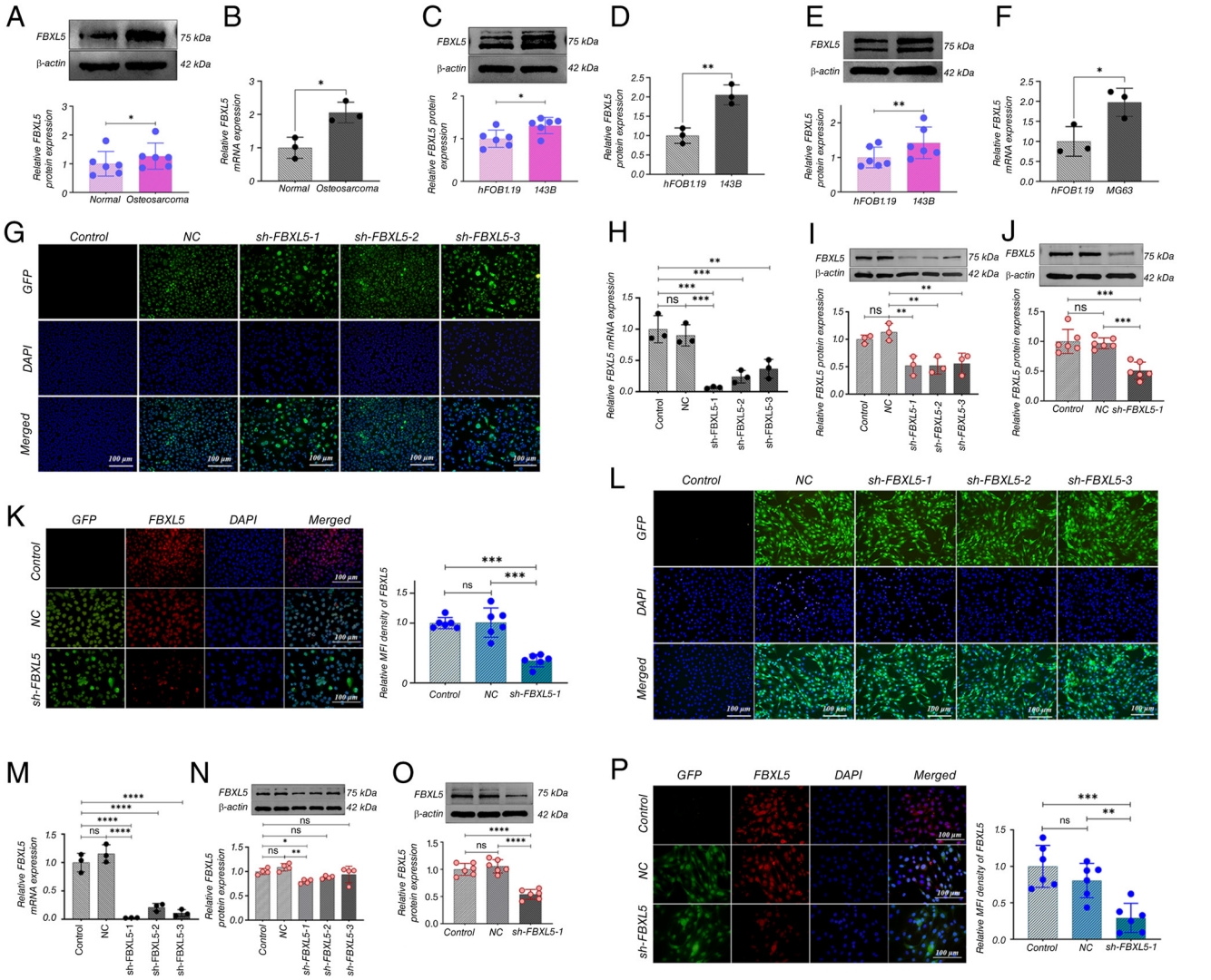

Figure 1. FBXL5 expression in OS tissues and cells and establishment of stable knockdown cell lines. (A) Western blot analysis of FBXL5 protein expression in OS cell lines; statistical analyses shown. (B) qPCR measurement of FBXL5 mRNA expression levels (n=3). (C) Western blot of FBXL5 in 143B cells. (D) qPCR of FBXL5 mRNA in 143B cells. (E) Western blot of FBXL5 in MG63 cells. (F) qPCR of FBXL5 mRNA in MG63 cells (n=3). (G) Lentiviral infection efficiency in 143B cells. (H) FBXL5 mRNA levels in 143B knockdown groups (n=3). (I) FBXL5 protein expression in 143B groups. (J) FBXL5 protein quantification in 143B groups. (K) Immunofluorescence staining of FBXL5 in 143B cells (scale bar, 100 μm). (L) Lentiviral infection, (M) mRNA, (N) protein expression and (O) quantification, and (P) immunofluorescence in MG63 cells (scale bar, 100 μm). n=3; *P<0.05, **P<0.01, ***P<0.001, ****P<0.0001. FBXL5, F-box and leucine-rich repeat protein 5; OS, osteosarcoma; WB, Western blot; qPCR, quantitative PCR; sh-, short hairpin; NC, negative control; GFP, green fluorescent protein.

Knockdown of FBXL5 inhibits the proliferation of 143B and MG63 cells. WB analysis and immunofluorescence were used to detect changes in expression of the proliferation-related proteins PCNA, CDK4 and cyclin D1 after FBXL5 knockdown, with EdU and CCK-8 assays assessing the impact on cell proliferation.

WB analysis showed a significant downregulation of PCNA, CDK4 and cyclin D1 protein expression levels in the sh-FBXL5 group compared with the control and NC groups in 143B (Fig. 2A-C) and MG63 (Fig. 2I-K) cells. Immunofluorescence analysis further confirmed a significant reduction in the mean fluorescence intensity of these proteins in the sh-FBXL5 group in both 143B (Fig. 2D-F) and MG63 (Fig. 2L-N) cells.

The EdU assay revealed a significant decrease in the number and proportion of EdU-positive cells in the sh-FBXL5 group in 143B (Fig. 2G) and MG63 (Fig. 2O) cells compared to the control and NC groups.

CCK-8 proliferation assays showed that sh-FBXL5 significantly inhibited the proliferation of 143B (Fig. 2H) and MG63 (Fig. 2P) cells, with notably lower optical density values compared to controls starting at 24 h; no significant differences were observed between the control and NC groups. These findings suggest that FBXL5 serves a key role in promoting OS cell proliferation, and its depletion suppresses tumor cell growth through downregulation of PCNA, CDK4 and cyclin D1.

FBXL5 knockdown promotes apoptosis in 143B and MG63 cells. WB analysis was used to analyze the expression changes of apoptosis-related proteins following FBXL5 knockdown, while the TUNEL assay assessed cell apoptosis.

The results showed that in the sh-FBXL5 group, expression of the anti-apoptotic protein Bcl-2 was significantly reduced, while the pro-apoptotic proteins BAX and caspase-3 were significantly increased in both 143B (Fig. 3A-C) and MG63

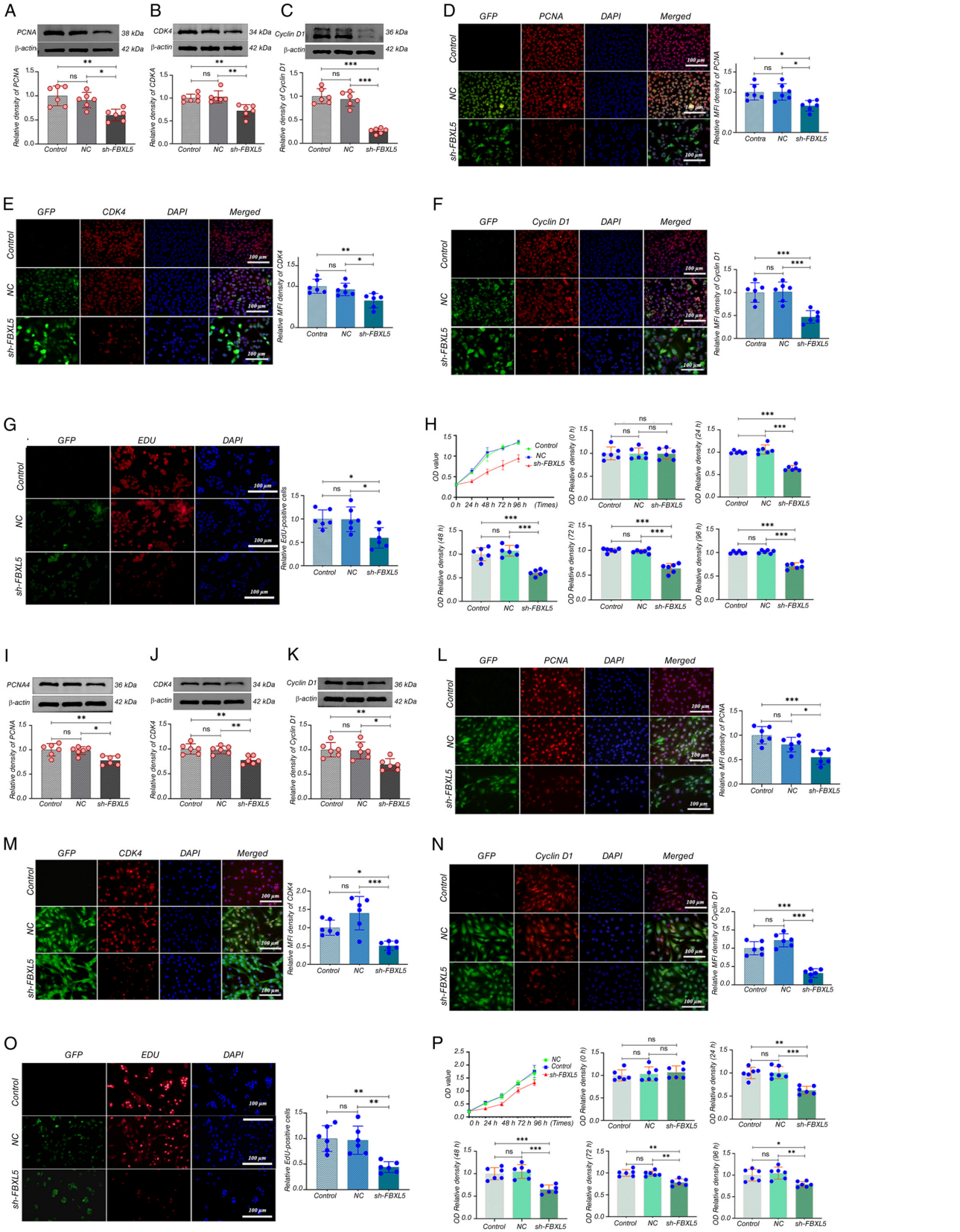

Figure 2. FBXL5 knockdown inhibits OS cell proliferation and downregulates cell cycle-related proteins. (A) WB analysis of PCNA protein expression in 143B cells after FBXL5 knockdown. (B) CDK4 expression by WB in 143B cells. (C) Cyclin D1 expression by WB in 143B cells. Immunofluorescence staining (red) of (D) PCNA, (E) CDK4 and (F) cyclin D1 in 143B cells; quantified using MFI (scale bar, 100 μm). (G) EdU assay in 143B cells showing proliferation; EdU-positive cells in red; quantification shown on the right. (H) CCK-8 cell proliferation assay in 143B cells with quantification of cell viability at different time points. WB analysis of (I) PCNA, (J) CDK4 and (K) cyclin D1 in MG63 cells after FBXL5 knockdown. Immunofluorescence staining (red) of (L) PCNA, (M) CDK4 and (N) cyclin D1 in MG63 cells; quantified by MFI (scale bar, 100 μm). (O) EdU assay showing proliferation in MG63 cells. (P) CCK-8 proliferation curve with quantification in MG63 cells. n=6; *P<0.05, **P<0.01, ***P<0.001. MFI, mean fluorescence intensity; PCNA, proliferating cell nuclear antigen; CDK4, cyclin-dependent kinase 4; GFP, green fluorescent protein; NC, negative control; FBXL5, F-box and leucine-rich repeat protein 5; OS, osteosarcoma; OD, optical density; sh-, short hairpin; WB, western blot; CCK-8, Cell Counting Kit-8.

(Fig. 3E-G) cells. TUNEL staining revealed nuclear fragmentation and morphological abnormalities in the sh-FBXL5 group, with intense red fluorescence signals (Fig. 3D and H). The proportion of TUNEL-positive cells was significantly higher in the sh-FBXL5 group compared with the control and NC groups, whereas there was no statistical difference observed between the control and NC groups.

This indicates that FBXL5 knockdown induces apoptosis in OS cells, suggesting that FBXL5 may function as an anti-apoptotic factor in osteosarcoma by upregulating Bcl-2 and downregulating BAX and caspase-3.

Knockdown of FBXL5 inhibits the migration and invasion abilities of 143B and MG63 cells. WB analysis was performed to detect changes in the expression of migration and invasion markers MMP2 and MMP9 following FBXL5 knockdown, and a wound healing assay was used to evaluate cell migration ability.

The results showed that MMP2 and MMP9 protein expression were significantly reduced in both 143B (Fig. 4A and B) and MG63 (Fig. 4E and F) cells in the sh-FBXL5 group compared with both the control and NC groups. The wound healing assay demonstrated that 143B (Fig. 4C) and MG63 (Fig. 4G) cells in the control and NC groups migrated markedly more quickly when compared with the sh-FBXL5 group; wound healing was significantly delayed at all time points in the sh-FBXL5 group, with incomplete wound closure at 96 h. The migration distance curve revealed that the migration distance of 143B (Fig. 4D) and MG63 (Fig. 4H) cells in the sh-FBXL5 group was significantly lower than that of the control group at all time points from 24 to 96 h.

These results imply that FBXL5 is involved in regulating OS cell migration and invasion, likely through the downregulation of MMP2 and MMP9, and targeting FBXL5 may limit metastatic potential.

Subcutaneous tumor xenograft model in nude mice. A subcutaneous tumor implantation model in nude mice was used to systematically assess the impact of FBXL5 knockdown on tumor growth, thereby investigating the role of FBXL5 in OS progression.

FBXL5 knockdown inhibits tumor growth. i) Body weight changes. In the sh-FBXL5 group, the body weight of nude mice in 143B (Fig. 5B) and MG63 (Fig. 5G) xenograft models remained stable, with a slight increase. By contrast, mice in the control and NC groups showed a slight weight increase during the first 10 days, followed by a continuous decline from day 14 onward.

ii) Tumor volume. Tumor formation was observed in all groups by day 10 post-implantation. Tumor volumes of 143B (Fig. 5D) and MG63 (Fig. 5I) in the sh-FBXL5 group were significantly smaller than those in the control group, with a marked reduction in growth rate at each time point.

iii) Tumor weight and morphology. At the study endpoint, gross tumor images showed that tumors in both the control and NC groups exhibited tight adhesion to the ribcage, whereas the sh-FBXL5 group displayed well-encapsulated tumors with no apparent invasion in both the 143B and MG63 xenograft models (Fig. 5A and F). Tumor weights and volumes of 143B (Fig. 5C and E) and MG63 (Fig. 5H and J) in the sh-FBXL5 group were significantly lower than those in the control group.

Histological analysis of transplanted tumors. Immunofluorescence analysis confirmed that in both the 143B (Fig. 6A and B) and MG63 (Fig. 6D and E) tumor models, FBXL5 expression was significantly reduced in the sh-FBXL5 group compared to the control and NC groups, confirming that lentivirus-mediated FBXL5 knockdown remained stable *in vivo*.

Hematoxylin and eosin staining showed that 143B (Fig. 6C) and MG63 (Fig. 6F) tumors in the control and NC groups exhibited characteristic malignant features, including disorganized cell arrangement, nest-like or diffuse distribution, variable morphology, uneven nuclear staining, frequent mitotic figures, marked atypia, unclear tissue boundaries, and extensive areas of necrosis and neovascularization. By contrast, tumors in the sh-FBXL5 group displayed more organized cell arrangement, relatively uniform morphology, even nuclear staining, fewer mitotic figures, reduced atypia, clear tissue boundaries, and significantly less necrosis and neovascularization.

Histological analysis confirmed that FBXL5 knockdown reduces malignant features of OS tumors *in vivo*, including disorganized cell arrangement, necrosis and neovascularization, further supporting its tumor-suppressive role.

Transcriptome sequencing analysis to explore the molecular mechanisms by which FBXL5 knockdown inhibits OS progression. RNA-seq was employed to analyze the transcriptomic changes in 143B and MG63 cell lines following FBXL5 knockdown to further investigate the molecular mechanisms through which FBXL5 knockdown inhibits OS progression.

Gene expression distribution and differential analysis. Following transcripts per million normalization, the gene expression distributions in 143B (Fig. 7A) and MG63 (Fig. 7G) cells exhibited normal distributions with high overlap, indicating high data quality. Volcano plot analysis revealed that, following FBXL5 knockdown, 3,039 genes were upregulated and 2,472 genes were downregulated in 143B cells (Fig. 7B), while in MG63 cells, 2,740 genes were upregulated and 1,776 genes were downregulated (Fig. 7H) ($P<0.05$, $|\log_2 FC|>1$). These GO enrichment results indicate that FBXL5 primarily affects metabolic and proliferation-related biological processes in OS cells.

GO enrichment analysis. GO enrichment analysis revealed that the differentially expressed genes were primarily enriched in biological processes such as ‘metabolic process’, ‘cellular process’, ‘immune system process’ and ‘growth’. In the cellular component category, the genes were mainly associated with ‘protein complex’ and ‘intracellular anatomical structure’, while in the molecular function category, they were enriched in ‘catalytic activity’ and ‘binding’ (Fig. 7C and I). Enrichment ratio analysis indicated that metabolism- and proliferation-related pathways were the most prominent (Fig. 7D and J), suggesting that FBXL5 regulates OS progression by modulating these pathways.

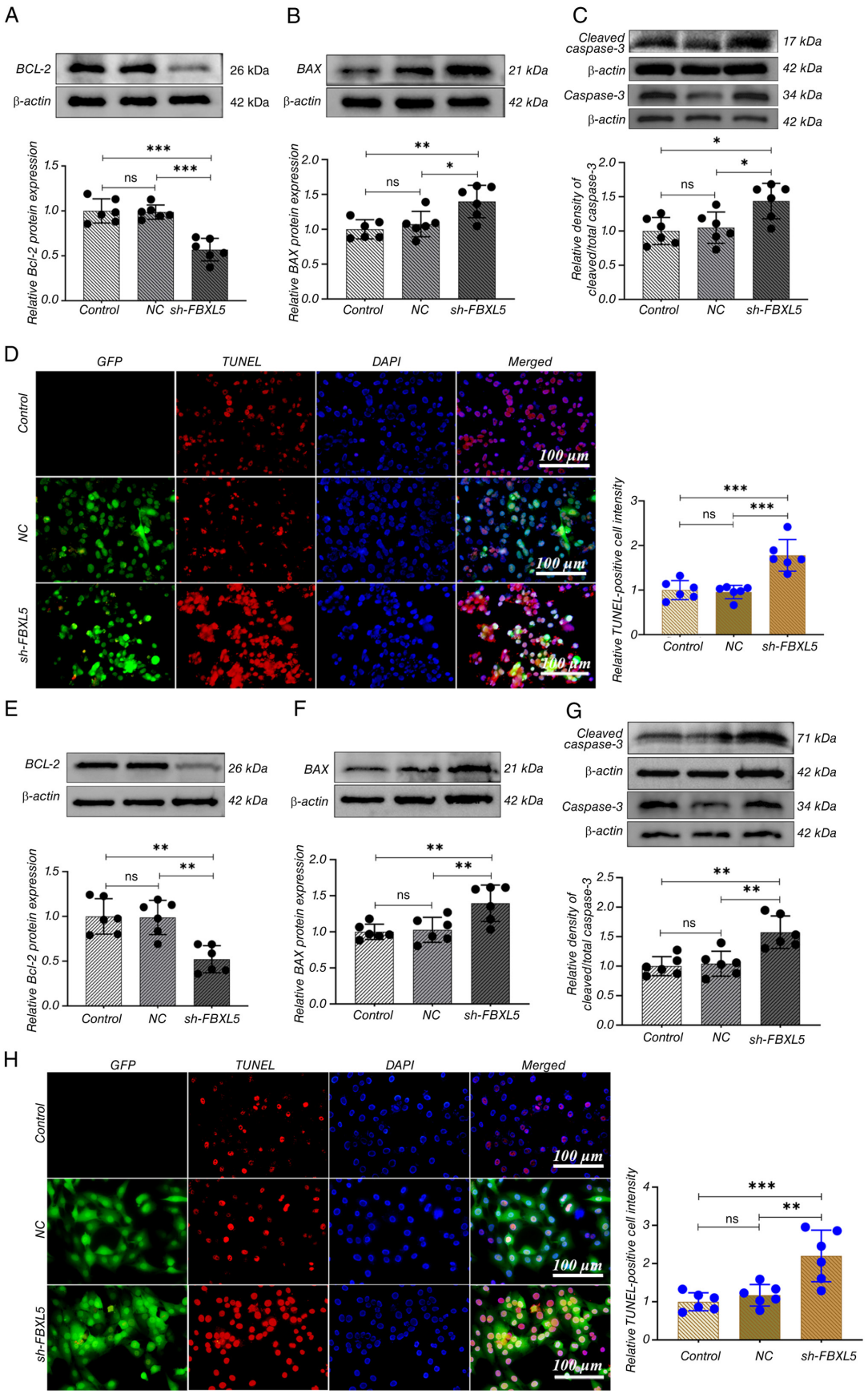

Figure 3. FBXL5 knockdown promotes OS cell apoptosis. (A) WB analysis of Bcl-2 protein expression in 143B cells after FBXL5 knockdown. (B) WB analysis of BAX protein expression in 143B cells. (C) WB analysis of caspase-3 protein expression in 143B cells. (D) TUNEL staining of 143B cells with quantification of TUNEL-positive cell intensity (scale bar, 100 μm). (E) WB analysis of Bcl-2 protein expression in MG63 cells after FBXL5 knockdown. (F) WB analysis of BAX protein expression in MG63 cells. (G) WB analysis of caspase-3 protein expression in MG63 cells. (H) TUNEL staining of MG63 cells with quantification of TUNEL-positive cell intensity (scale bar, 100 μm). n=6; *P<0.05, **P<0.01, ***P<0.001. OS, osteosarcoma; WB, western blot; Bcl-2, B-cell lymphoma 2; FBXL5, F-box and leucine-rich repeat protein 5.

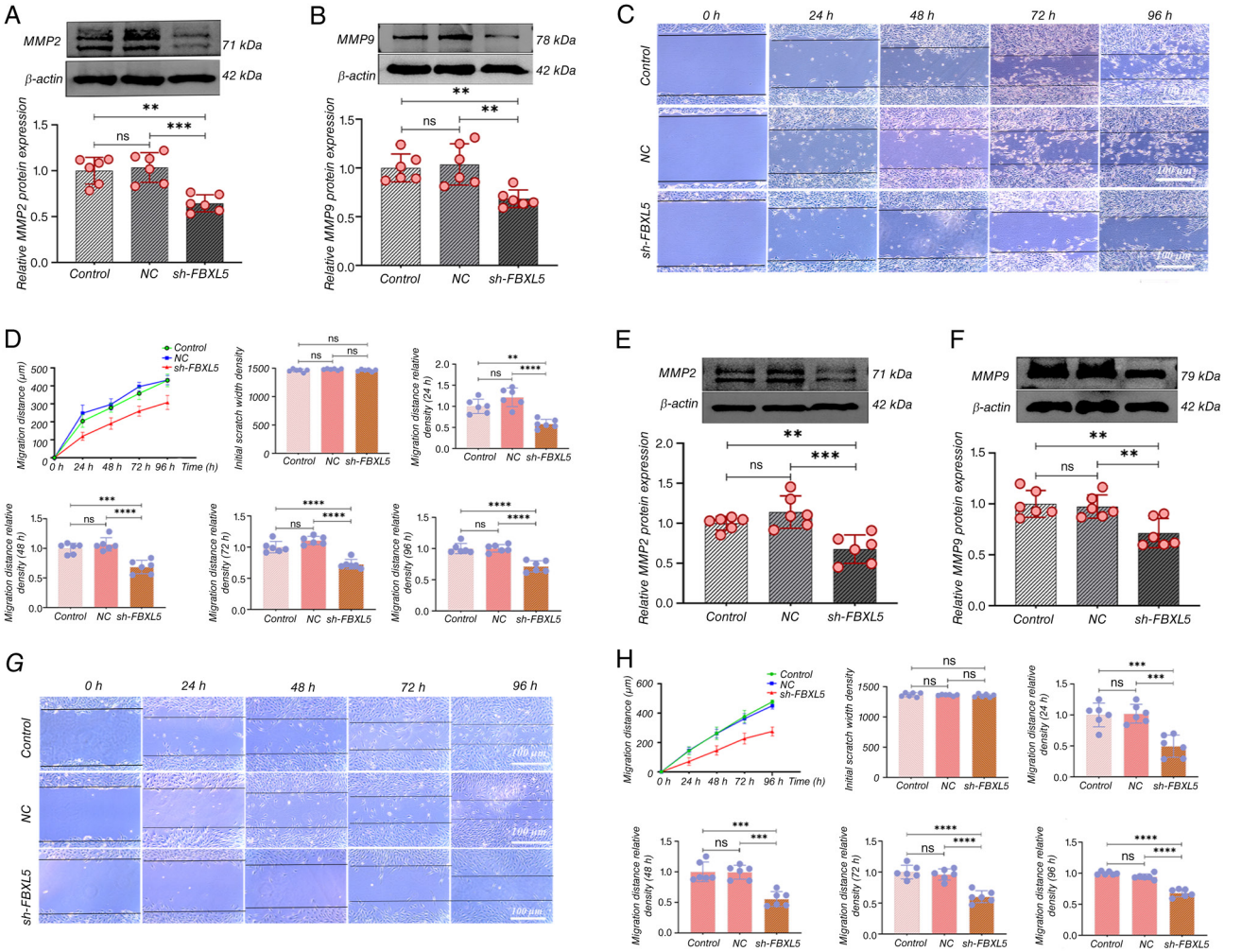

Figure 4. FBXL5 knockdown inhibits OS cell migration ability and migration-related protein expression. (A) WB analysis of MMP2 protein expression in 143B cells after FBXL5 knockdown. (B) WB analysis of MMP9 protein expression in 143B cells. (C) Wound healing assay in 143B cells from 0 to 96 h; wound width measured using a dashed line at the edge of the wound (scale bar, 100 μm). (D) Quantification of migration distance at different time points in 143B cells. (E) WB analysis of MMP2 in MG63 cells after FBXL5 knockdown. (F) WB analysis of MMP9 in MG63 cells. (G) Wound healing assay in MG63 cells from 0 to 96 h; wound width measured using a dashed line at the edge of the wound (scale bar, 100 μm). (H) Quantification of migration distance at different time points in MG63 cells. n=6; **P<0.01, ***P<0.001, ****P<0.0001. FBXL5, F-box and leucine-rich repeat protein 5; OS, osteosarcoma; WB, western blot; NC, negative control; sh-, short hairpin.

KEGG enrichment analysis. KEGG enrichment analysis revealed that the differentially expressed genes were significantly enriched in the 'MAPK signaling pathway-plant' (Fig. 7E and K). In the sh-FBXL5 cells, the expression levels of proliferation-related genes (PCNA, cyclin D1 and CDK4) were significantly downregulated, and alterations in the expression of MAPK pathway members [MAPK8, dual specificity phosphatase 2 (DUSP2)] were observed. Notably, the downregulation of DUSP2 may be associated with altered ERK activity and suppressed proliferative signaling; however, the direct regulatory relationship requires further investigation (Fig. 7F and L).

KEGG pathway analysis identified the MAPK signaling pathway as significantly enriched following FBXL5 knockdown, highlighting this pathway as a key mediator of FBXL5's oncogenic functions in OS (Fig. 7E and K).

MEK/ERK signaling pathway validation. WB analysis showed that after FBXL5 knockdown, the expression levels of Ras, Raf, MEK1/2 and ERK1/2 proteins were significantly reduced in 143B (Fig. 8A-D) and MG63 (Fig. 8I-L) cells. Immunofluorescence further confirmed that the expression of MEK1/2 and ERK1/2 was markedly decreased in 143B (Fig. 8E and F) and MG63 (Fig. 8M and N) cells. Immunohistochemistry of xenograft tumors revealed that Raf and MEK1/2 expression levels were significantly reduced in the sh-FBXL5 group in both 143B (Fig. 8G and H) and MG63 (Fig. 8O and P) models.

Collectively, these data demonstrate that FBXL5 knockdown suppresses OS progression by inhibiting the MAPK/ERK signaling pathway at multiple levels (Ras, Raf, MEK and ERK), providing a mechanistic basis for its tumor-suppressive effects.

Discussion

Surgical resection combined with chemotherapy remains the standard treatment for OS, but metastasis, drug resistance and poor prognosis continue to present significant clinical challenges (19-21). The 5-year survival rate for localized OS is ~60%, while it remains under 20% for metastatic cases (22,23). Current chemotherapy regimens offer limited efficacy, and

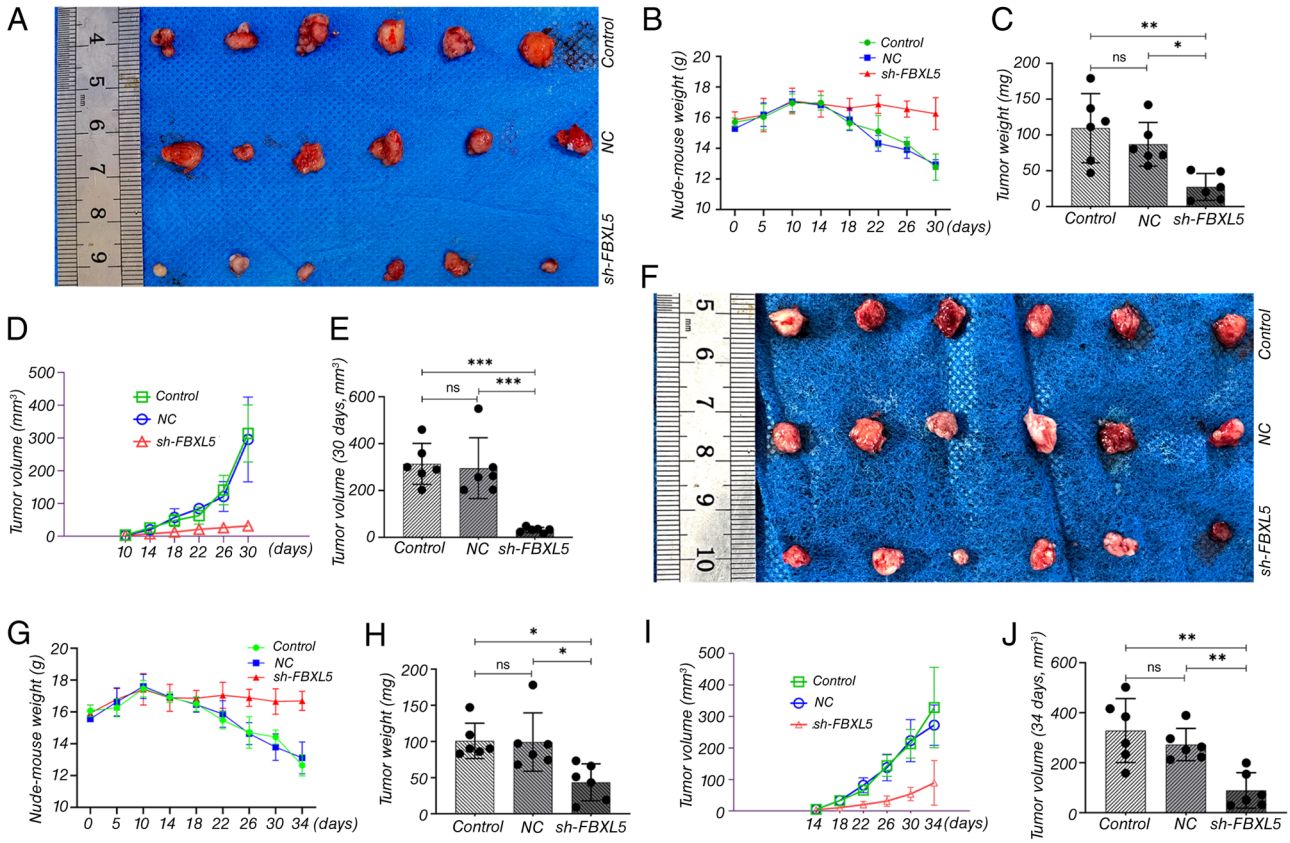

Figure 5. FBXL5 knockdown inhibits OS cell tumorigenicity in nude mice. (A) Tumor morphology comparison in each group 30 days after 143B cell implantation. (B) Body weight change curve of nude mice implanted with 143B cells. (C) Comparison of final tumor weight in 143B xenografts. (D) Tumor volume growth curve in 143B xenografts. (E) Comparison of final tumor volume in 143B xenografts. (F) Tumor morphology comparison in each group 34 days after MG63 cell implantation. (G) Body weight change curve of nude mice implanted with MG63 cells. (H) Comparison of final tumor weight in MG63 xenografts. (I) Tumor volume growth curve in MG63 xenografts. (J) Comparison of final tumor volume in MG63 xenografts. n=6; *P<0.05, **P<0.01, ***P<0.001. FBXL5, F-box and leucine-rich repeat protein 5; OS, osteosarcoma; WB, western blot; NC, negative control; sh-, short hairpin.

although targeted therapies are recommended by the National Comprehensive Cancer Network, they have not substantially improved the overall survival rate of patients (24,25). Thus, identifying novel molecular mechanisms and therapeutic targets is essential. The present study investigated the role of the E3 ubiquitin ligase FBXL5 in OS, specifically focusing on its signaling pathways and regulatory effects on OS cancer cell behavior.

As an E3 ubiquitin ligase that regulates iron homeostasis, FBXL5 serves a complex role in various cancers, functioning as either an oncogene or tumor suppressor (26). In gastric cancer, overexpression of FBXL5 significantly reduces metastatic potential, while its knockdown enhances Snail1 stability, promoting cell migration (27-30). By contrast, the present study revealed that FBXL5 expression was significantly elevated in OS. In a lung cancer model, FBXL5 knockout induced iron accumulation, which inhibited p27^Kip1 degradation and caused G1/S-phase cell cycle arrest, ultimately suppressing tumor growth (10,31). Clinical studies indicate that ~19% of patients with hepatocellular carcinoma show low FBXL5 expression, which correlates with a poor prognosis (12,32). In advanced-stage ccRCC, ~30% of patients exhibit reduced FBXL5 expression, which is significantly associated with poorer survival (hazard ratio ~2.0) (33). These findings highlight the variable expression of FBXL5 between normal and tumor tissues across malignancies, suggesting its potential as a prognostic biomarker for various cancers, including OS.

FBXL5 functions at the intersection of iron metabolism and cellular signaling pathways (34). In gastric cancer, FBXL5 inhibits the EMT by mediating the ubiquitination and degradation of Snail1 and cortactin, while also reducing the stability of human single-stranded DNA-binding protein 1 (27,28,35). In OS, FBXL5 predominantly regulates cell cycle progression and survival. The present study demonstrated that FBXL5 knockdown suppressed cell proliferation by downregulating the expression of PCNA, cyclin D1 and CDK4. FBXL5 deficiency increases IRP2 activity, disrupts iron homeostasis and causes reactive oxygen species (ROS) accumulation, stabilizing p27 and inducing G1-phase arrest (12,31,36). Furthermore, FBXL5 knockdown reduced the expression of MMP2 and MMP9, significantly impairing cell migration. Consequently, FBXL5 can act as an oncogene or tumor suppressor, depending on the specific molecular pathways it regulates in different cancers.

The present study found that FBXL5 knockdown was associated with a significant reduction in MAPK/ERK signaling activity in OS models. RNA-seq and experimental validation revealed that FBXL5 silencing led to a marked decrease in the phosphorylation levels of ERK1/2 (37,38). Although FBXL5 may modulate negative regulators of the MAPK pathway, such as sprouty RTK signaling antagonist 2 or DUSP

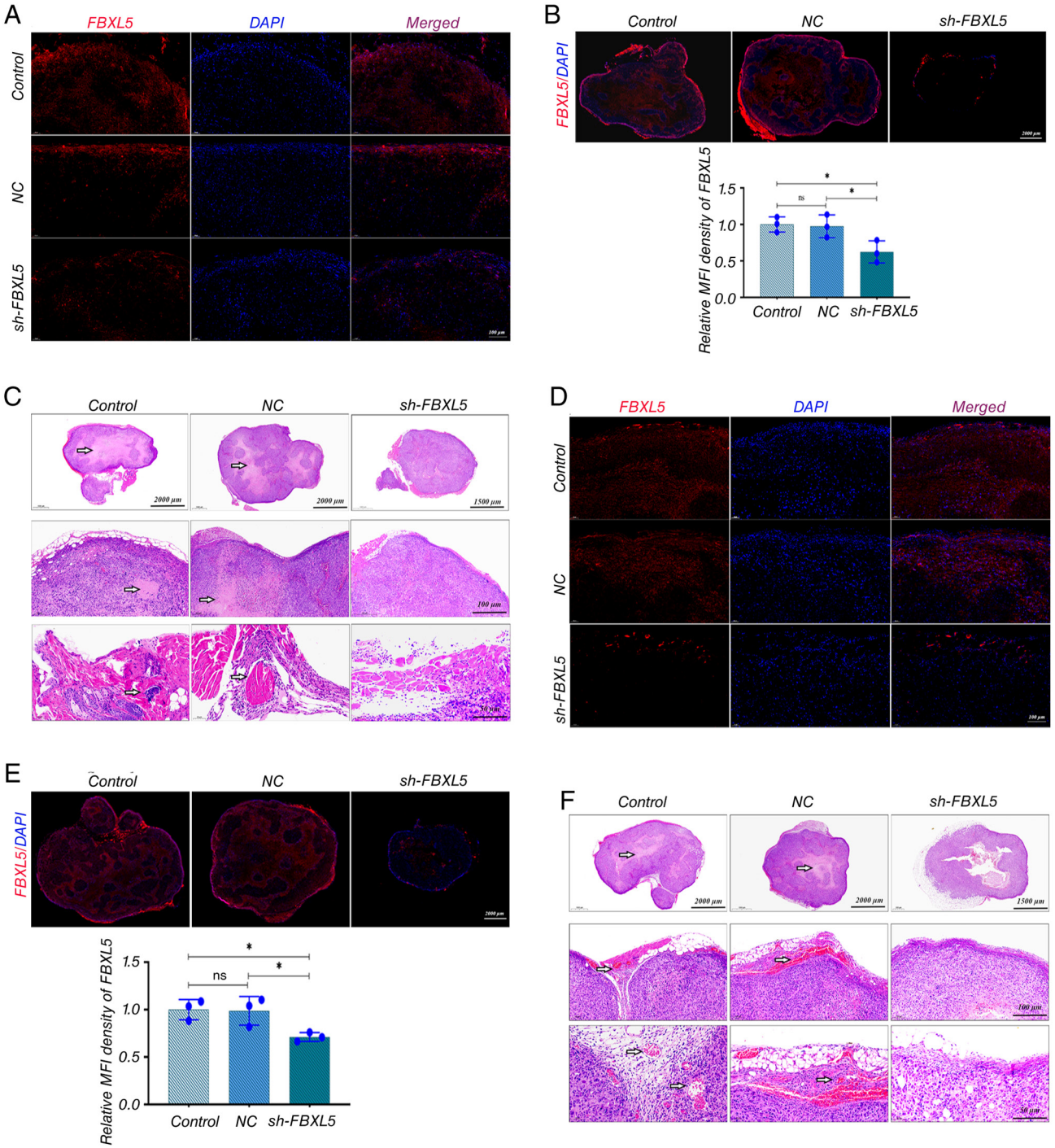

Figure 6. *In vivo* stability verification of FBXL5 knockdown and H&E staining of xenograft tumors. (A) IF staining of FBXL5 protein in tumor tissues from each group in the 143B nude mouse model. (B) Quantification of FBXL5 fluorescence intensity in 143B tumors; y-axis represents relative MFI density of FBXL5. (C) H&E staining of 143B tumor tissues from each group; top row, low magnification; middle row, medium magnification; bottom row, high magnification. (D) IF staining of FBXL5 protein in tumor tissues from each group in the MG63 nude mouse model. (E) Quantification of FBXL5 fluorescence intensity in MG63 tumors; y-axis represents relative MFI density of FBXL5. (F) H&E staining of MG63 tumor tissues from each group; top row, low magnification; middle row, medium magnification; bottom row, high magnification. Arrows indicate cells with high FBXL5 expression. n=6; *P<0.05. FBXL5, F-box and leucine-rich repeat protein 5; HE, hematoxylin and eosin; NC, negative control; sh-, short hairpin; IF, immunofluorescence.

family members, this proposed mechanism is speculative and requires direct experimental validation (39). The disruption of iron homeostasis and increased ROS levels induced by FBXL5 knockdown may further suppress ERK pathway activity by activating stress pathways such as p38/c-Jun N-terminal kinase (38). While the present study does not explicitly confirm that p21 influences the ERK signaling in OS cells through this mechanism, further research is warranted to clarify the specific role of FBXL5 in regulating MAPK signaling.

Research suggests that FBXL5 modulates ferroptosis and other signaling pathways, such as iron homeostasis and ROS-mediated signaling (40,41). As an iron-dependent form of programmed cell death characterized by lipid peroxidation, ferroptosis represents a potential therapeutic target for

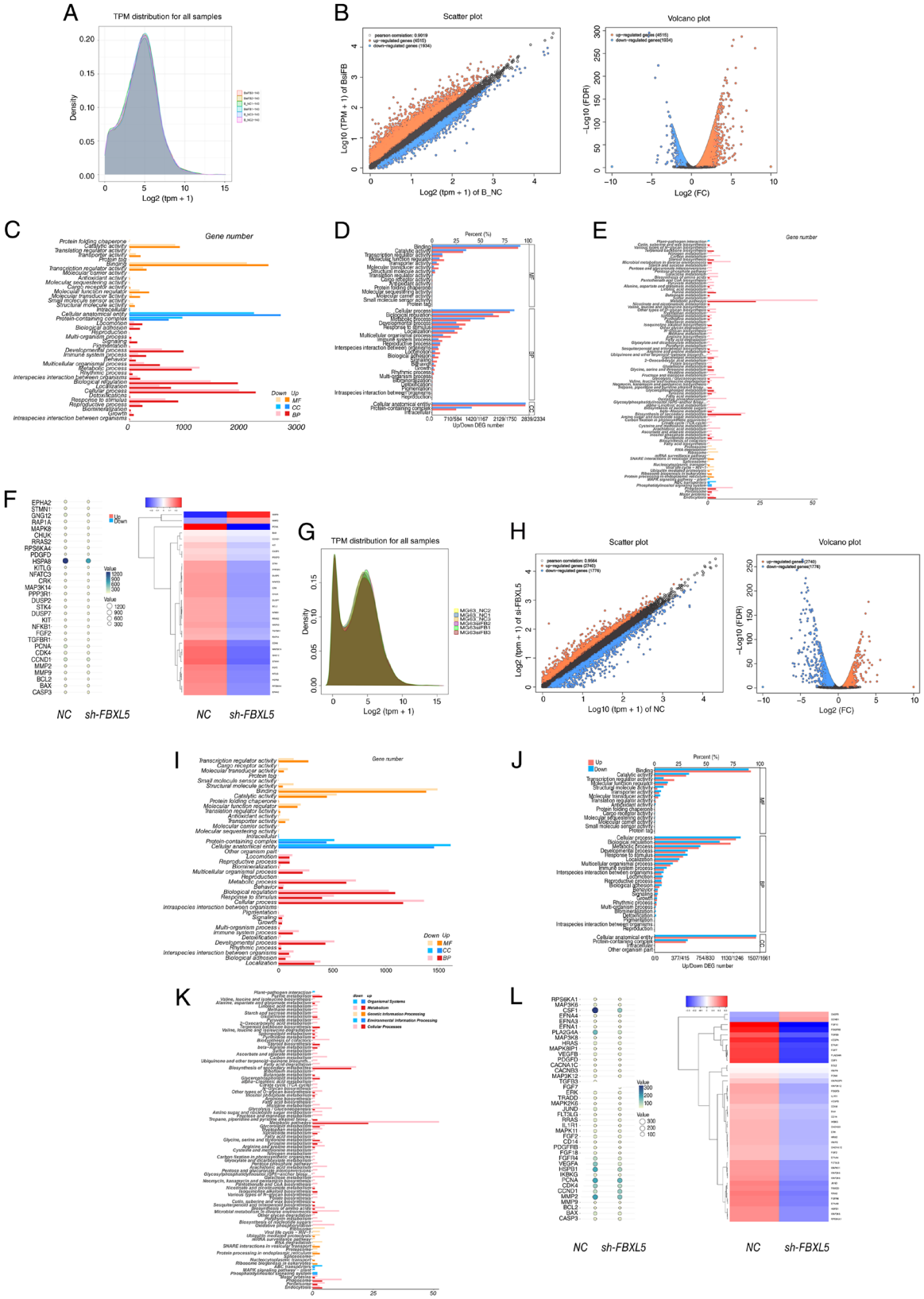

Figure 7. Effect of FBXL5 knockdown on the transcriptomes of 143B and MG63 OS cell lines. (A) Gene expression density distribution curve of 143B cells after TPM normalization. (B) Volcano plot of differentially expressed genes in 143B cells following FBXL5 knockdown. (C) Bar graph of GO enrichment analysis for differentially expressed genes in 143B cells. (D) GO enrichment ratio plot showing that metabolism- and proliferation-related pathways have the highest proportions in 143B cells; (E) KEGG enrichment analysis revealing significant enrichment of the MAPK signaling pathway in 143B cells. (F) Heatmap analysis of genes related to the MAPK signaling pathway in 143B cells. (G) Gene expression density distribution curve of MG63 cells after TPM normalization. (H) Volcano plot of differentially expressed genes in MG63 cells following FBXL5 knockdown. (I) Bar graph of GO enrichment analysis for differentially expressed genes in MG63 cells. (J) GO enrichment ratio plot showing that metabolism- and proliferation-related pathways have the highest proportions in MG63 cells. (K) KEGG enrichment analysis revealing significant enrichment of the MAPK signaling pathway in MG63 cells. (L) Heatmap analysis of genes related to the MAPK signaling pathway in MG63 cells. FBXL5, F-box and leucine-rich repeat protein 5; OS, osteosarcoma; TPM, transcripts per million; KEGG, Kyoto Encyclopedia of Genes and Genomes; GO, Gene Ontology.

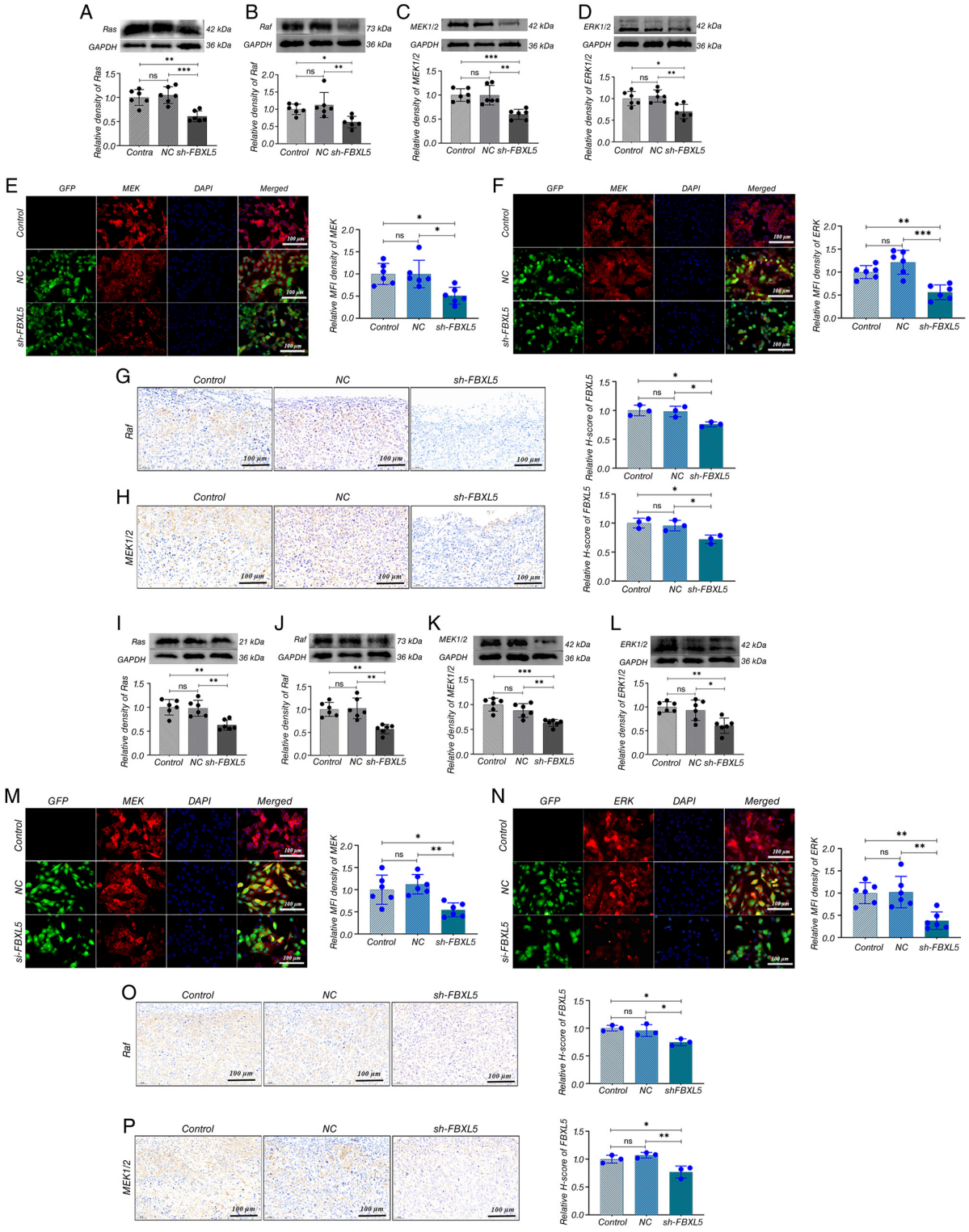

Figure 8. FBXL5 knockdown suppresses the Ras/Raf/MEK/ERK signaling cascade in OS cells. Immunoblot analysis and quantification of (A) Ras, (B) Raf, (C) MEK1/2 and (D) ERK1/2 proteins in 143B cells; y-axis represents relative density. IF staining of (E) MEK1/2 and (F) ERK1/2 in 143B cells (green, GFP-positive transfected cells; red, target protein; blue, DAPI-stained nuclei; scale bar, 100 μm). IHC staining and semi-quantitative analysis of (G) Raf and (H) MEK1/2 in 143B xenograft tumors (scale bar, 100 μm). Immunoblot analysis and quantification of (I) Ras, (J) Raf, (K) MEK1/2 and (L) ERK1/2 in MG63 cells; y-axis represents relative density. IF staining of (M) MEK1/2 and (N) ERK1/2 in MG63 cells (scale bar, 100 μm). IHC staining of (O) Raf and (P) MEK1/2 in MG63 xenograft tumors (scale bar, 100 μm). n=6; *P<0.05, **P<0.01, ***P<0.001. OS, osteosarcoma; GFP, green fluorescent protein; NC, negative control; sh-, short hairpin; FBXL5, F-box and leucine-rich repeat protein 5; ns, not significant; IF, immunofluorescence; IHC, immunohistochemical.

malignant tumors such as OS (42). High FBXL5 expression limits iron and ROS accumulation, inhibiting ferroptosis. Conversely, inducing ferroptosis has been shown to effectively eradicate drug-resistant cells and OS stem cells (42-44). Additionally, FBXL5 may modulate the crosstalk between EMT and nuclear factor κB (NF-κB) signaling by inducing Snail1 degradation (28,45,46) or regulating β-transducin repeat-containing protein to influence NF-kB activity (47).

Targeted strategies involving FBXL5 in OS may leverage insights gained from successful mouse double minute 2-p53 inhibitor therapies (48,49). One potential approach is to simulate a pseudo-iron deficiency by utilizing iron chelators to activate FBXL5's iron-responsive domain, triggering its self-ubiquitination and degradation (36). This mimics the effects of FBXL5 knockdown, thereby inhibiting tumor cell proliferation or inducing ferroptosis (40,50). Iron chelators such as deferoxamine are established clinical treatments for iron overload diseases (51,52), and are currently being investigated as adjunctive therapies for cancer (53). Similarly, ferroptosis-inducing agents such as RSL3 and erastin can be combined with chemotherapy (42,54). FBXL5 expression levels may serve as a predictor of therapeutic responses, with higher expression potentially indicating increased resistance to chemo- and radiotherapy. Modulating the FBXL5-iron homeostasis axis holds promise for enhancing radiosensitivity (55-57).

Overall, FBXL5 serves a multifaceted role in the progression of OS by promoting cell proliferation and migration through both direct substrate degradation and indirect modulation of iron homeostasis and ROS levels. The present study reveals a previously unrecognized link between FBXL5 and the MAPK/ERK signaling pathway, broadening the understanding of its function and suggesting novel therapeutic targets. To more fully understand the molecular mechanisms by which FBXL5 regulates OS progression, future research should involve screening interacting proteins via co-immunoprecipitation mass spectrometry and performing gene rescue experiments.

In conclusion, the present study suggests that FBXL5 promotes tumor growth in OS by activating the MAPK/ERK signaling pathway. The results indicated that FBXL5 promoted tumor cell proliferation and migration by maintaining iron homeostasis and activating the MAPK/ERK signaling pathway. This tissue-specific function contradicts the anti-cancer role observed in epithelial tumors. The reveal that FBXL5 modulates the MAPK/ERK pathway not only broadens the functional knowledge of this protein but also offers a novel potential therapeutic avenue for treating OS. Leveraging the iron-responsive properties of FBXL5, iron chelator-induced degradation is a promising treatment strategy. Future studies should validate FBXL5 expression in larger cohorts to confirm its prognostic and therapeutic value in OS. Furthermore, an investigation into combining FBXL5 inhibition with ferroptosis inducers or MEK inhibitors is warranted. This study provides key evidence for understanding the molecular mechanisms of OS and developing new therapeutic strategies.

The present study demonstrated that FBXL5 knockdown inhibited the progression of OS through multiple mechanisms. *In vitro* experiments confirmed that FBXL5 knockdown suppressed cell proliferation, induced apoptosis and reduced migration and invasion. In the xenograft model, FBXL5 knockdown significantly inhibited tumor growth, reduced tumor volume and weight, and improved the physiological condition of tumor-bearing mice. Histopathological analysis showed that FBXL5 knockdown reduced tumor malignancy, as evidenced by decreased cellular atypia, clear tissue boundaries and reduced necrosis and neovascularization. The *in vitro* and *in vivo* data consistently indicate that FBXL5 serves a functional role in regulating the malignant biological behaviors of OS.

Limitations of the present study include limited clinical sample size (n=6), warranting validation in larger cohorts. The exact molecular mechanism by which FBXL5 regulates the MAPK/ERK pathway remains incompletely understood. *In vivo* experiments were limited to subcutaneous xenograft models, which may not fully represent OS metastasis. Additionally, shRNA-mediated knockdown was the primary method used; alternative approaches are needed to confirm the results.

Acknowledgements

Not applicable.

Funding

This work was supported by the National Natural Science Foundation of China (grant no. 82360435), the Lanzhou University Second Hospital Cuiying Youth Fund Project (grant no. CY2022-QN-A03), the Cuiying Science and Technology Innovation Program Project (grant no. 2022-MS-A10), the Lanzhou Youth Science and Technology Talents Innovation Project (grant no. 2023-2-39) and the Natural Science Foundation of Gansu Province (grant no. 24JRRA1101).

Availability of data and materials

The RNA sequencing data generated in this study have been deposited in the NCBI BioProject database under BioProject accession number PRJNA1440046 and are publicly available at the following URL: https://www.ncbi.nlm.nih.gov/bioproject/PRJNA1440046. All other data supporting the findings of the present study are available from the corresponding author upon reasonable request.

Author's contributions

YCM and WMZ contributed equally to this work as first authors. YCM, WMZ and WN conceived and designed the study. YCM, WMZ, YQS and YBD performed the experiments, including cell culture, lentiviral transduction, qPCR, western blotting, immunofluorescence and animal studies. YCM, WMZ and HHZ analyzed and interpreted the data, including RNA-seq bioinformatics analysis. YCM and WMZ drafted the manuscript. HHZ and WN critically revised the manuscript for important intellectual content. WN and HHZ are co-corresponding authors. All authors read and approved the final manuscript, and agree to be accountable for all aspects of the work, ensuring that questions related to the accuracy or integrity of any part are appropriately investigated and resolved. YCM and WMZ confirm the authenticity of all the raw data.

Ethics approval and consent to participate

This study was conducted in accordance with the Declaration of Helsinki and approved by the Ethics Committee of the Second Hospital of Lanzhou University. Human tissue

samples collection was approved under ethics approval no. 2024A-504. Written informed consent was obtained from all adult patients or from the parents/legal guardians of patients under 18 years of age prior to sample collection and participation in the study. All animal experiments were approved by the Institutional Animal Care and Use Committee of Lanzhou University (approval no. D2024-417) and performed in accordance with the Guide for the Care and Use of Laboratory Animals.

Patient consent for publication

Written informed consent for publication of clinical details and clinical images was obtained from all patients or their parents/legal guardians for patients under 18 years of age. All patient information has been de-identified to protect patient privacy.

Competing interests

The authors declare that they have no competing interests.

References

1. Song K, Song J, Lin K, Chen F, Ma X, Jiang J and Li F: Survival analysis of patients with metastatic osteosarcoma: A surveillance, epidemiology, and end results population-based study. Int Orthop 43: 1983-1991, 2019.
2. Mettmann VL, Blattmann C, Friedel G, Harrabi S, von Kalle T, Kager L, Kevric M, Kühne T, Nathrath M, Sorg B, *et al*: Primary Multi-Systemic metastases in osteosarcoma: Presentation, treatment, and survival of 83 patients of the cooperative osteosarcoma study group. Cancers 16: 275, 2024.
3. Mao P, Feng Z, Liu Y, Zhang K, Zhao G, Lei Z, Di T and Zhang H: The role of ubiquitination in osteosarcoma development and therapies. Biomolecules 14: 791, 2024.
4. Xin S and Wei G: Prognostic factors in osteosarcoma: A study level meta-analysis and systematic review of current practice. J Bone Oncol 21: 100281, 2020.
5. Bishop MW, Janeway KA and Gorlick R: Future directions in the treatment of osteosarcoma. Curr Opin Pediatr 28: 26-33, 2016.
6. Zoumpoulidou G, Alvarez-Mendoza C, Mancusi C, Ahmed RM, Denman M, Steele CD, Tarabichi M, Roy E, Davies LR, Manji J, *et al*: Therapeutic vulnerability to PARP1,2 inhibition in RB1-mutant osteosarcoma. Nat Commun 12: 7064, 2021.
7. Sayles LC, Breese MR, Koehne AL, Leung SG, Lee AG, Liu HY, Spillinger A, Shah AT, Tanasa B, Straessler K, *et al*: Genome-informed targeted therapy for osteosarcoma. Cancer Discov 9: 46-63, 2019.
8. Muto Y, Nishiyama M, Nita A, Moroishi T and Nakayama KI: Essential role of FBXL5-mediated cellular iron homeostasis in maintenance of hematopoietic stem cells. Nat Commun 8: 16114, 2017.
9. Wang H, Shi H, Rajan M, Canarie ER, Hong S, Simoneschi D, Pagano M, Bush MF, Stoll S, Leibold EA and Zheng N: FBXL5 Regulates IRP2 stability in iron homeostasis via an Oxygen-responsive (2Fe2S) cluster. Mol Cell 78: 31-41.e5, 2020.
10. Chen ZW, Liu B, Tang NW, Xu YH, Ye XY, Li ZM, Niu XM, Shen SP, Lu S and Xu L: FBXL5-mediated degradation of single-stranded DNA-binding protein hSSB1 controls DNA damage response. Nucleic Acids Res 42: 11560-11569, 2014.
11. Bian X, Yin S, Yin X, Fang T, Wang Y, Yang S, Jiang X, Xue Y, Ye F and Zhang L: Clinical and biological significances of FBLN5 in gastric cancer. Cancers (Basel) 15: 553, 2023.
12. Muto Y, Moroishi T, Ichihara K, Nishiyama M, Shimizu H, Eguchi H, Moriya K, Koike K, Mimori K, Mori M, *et al*: Disruption of FBXL5-mediated cellular iron homeostasis promotes liver carcinogenesis. J Exp Med 216: 950-965, 2019.
13. He ZJ, Li W, Chen H, Wen J, Gao YF and Liu YJ: miR-1306-3p targets FBXL5 to promote metastasis of hepatocellular carcinoma through suppressing snail degradation. Biochem Biophys Res Commun 504: 820-826, 2018.
14. Chandhanayingyong C, Kim Y, Staples JR, Hahn C and Lee FY: MAPK/ERK signaling in osteosarcomas, Ewing sarcomas and chondrosarcomas: Therapeutic implications and future directions. Sarcoma 2012: 404810, 2012.
15. Gao Z, Zhao GS, Lv Y, Peng D, Tang X, Song H and Guo QN: Anoikis-resistant human osteosarcoma cells display significant angiogenesis by activating the Src kinase-mediated MAPK pathway. Oncol Rep 41: 235-245, 2019.
16. Liu W, Wang B, Duan A, Shen K, Zhang Q, Tang X, Wei Y, Tang J and Zhang S: Exosomal transfer of miR-769-5p promotes osteosarcoma proliferation and metastasis by targeting DUSP16. Cancer Cell Int 21: 541, 2021.
17. Noh K, Kim KO, Patel NR, Staples JR, Minematsu H, Nair K and Lee FY: Targeting inflammatory kinase as an adjuvant treatment for osteosarcomas. J Bone Joint Surg Am 93: 723-732, 2011.
18. Livak KJ and Schmittgen TD: Analysis of relative gene expression data using real-time quantitative PCR and the 2(-Delta Delta C(T)) method. Methods 25: 402-408, 2001.
19. Meltzer PS and Helman LJ: New horizons in the treatment of osteosarcoma. N Engl J Med 385: 2066-2076, 2021.
20. Tian H, Cao J, Li B, Nice EC, Mao H, Zhang Y and Huang C: Managing the immune microenvironment of osteosarcoma: The outlook for osteosarcoma treatment. Bone Res 11: 11, 2023.
21. Zhou Y, Yang D, Yang Q, Lv X, Huang W, Zhou Z, Wang Y, Zhang Z, Yuan T, Ding X, *et al*: Single-cell RNA landscape of intratumoral heterogeneity and immunosuppressive microenvironment in advanced osteosarcoma. Nat Commun 11: 6322, 2020.
22. Hu Z, Wen S, Huo Z, Wang Q, Zhao J, Wang Z, Chen Y, Zhang L, Zhou F, Guo Z, *et al*: Current status and prospects of targeted therapy for osteosarcoma. Cells 11: 3507, 2022.
23. Lu Y, Zhang J, Chen Y, Kang Y, Liao Z, He Y and Zhang C: Novel immunotherapies for osteosarcoma. Front Oncol 12: 830546, 2022.
24. Harris MA and Hawkins CJ: Recent and ongoing research into metastatic osteosarcoma treatments. Int J Mol Sci 23: 3817, 2022.
25. Duffaud F, Mir O, Boudou-Rouquette P, Piperno-Neumann S, Penel N, Bompas E, Delcambre C, Kalbacher E, Italiano A, Collard O, *et al*: Efficacy and safety of regorafenib in adult patients with metastatic osteosarcoma: A non-comparative, randomised, double-blind, placebo-controlled, phase 2 study. Lancet Oncol 20: 120-133, 2019.
26. Mayank AK, Pandey V, Vashisht AA, Barshop WD, Rayatpisheh S, Sharma T, Haque T, Powers DN and Wohlschlegel JA: An Oxygen-dependent interaction between FBXL5 and the CIA-targeting complex regulates iron homeostasis. Mol Cell 75: 382-393.e5, 2019.
27. Viñas-Castells R, Frías Á, Robles-Lanuza E, Zhang K, Longmore GD, García de Herreros A and Díaz VM: Nuclear ubiquitination by FBXL5 modulates Snail1 DNA binding and stability. Nucleic Acids Res 42: 1079-1094, 2014.
28. Gong J, Cao J, Liu G and Huo JR: Function and mechanism of F-box proteins in gastric cancer (review). Int J Oncol 47: 43-50, 2015.
29. Wang M, Dai W, Ke Z and Li Y: Functional roles of E3 ubiquitin ligases in gastric cancer. Oncol Lett 20: 22, 2020.
30. Wu W, Ding H, Cao J and Zhang W: FBXL5 inhibits metastasis of gastric cancer through suppressing Snail1. Cell Physiol Biochem 35: 1764-1772, 2015.
31. Hinokuma H, Kanamori Y, Ikeda K, Hao L, Maruno M, Yamane T, Maeda A, Nita A, Shimoda M, Niimura M, *et al*: Distinct functions between ferrous and ferric iron in lung cancer cell growth. Cancer Sci 114: 4355-4364, 2023.
32. Cho YA, Kim SE, Park CK, Koh HH, Park CK and Ha SY: Loss of F-Box and leucine rich repeat protein 5 (FBXL5) expression is associated with poor survival in patients with hepatocellular carcinoma after curative resection: A Two-institute study. Cancer Genomics Proteomics 20: 298-307, 2023.
33. Park CK, Heo J, Ham WS, Choi YD, Shin SJ and Cho NH: Ferroportin and FBXL5 as prognostic markers in advanced stage clear cell renal cell carcinoma. Cancer Res Treat 53: 1174-1183, 2021.
34. Wang H, Lu Y, Wang M, Wu Y, Wang X and Li Y: Roles of E3 ubiquitin ligases in gastric cancer carcinogenesis and their effects on cisplatin resistance. J Mol Med (Berl) 99: 193-212, 2021.
35. Liu C, Liu Y, Yu Y, Zhao Y and Yu A: Comprehensive analysis of ferroptosis-related genes and prognosis of cutaneous melanoma. BMC Med Genomics 15: 39, 2022.
36. Jiao Q, Du X, Wei J, Li Y and Jiang H: Oxidative stress regulated iron regulatory protein IRP2 through FBXL5-Mediated Ubiquitination-proteasome way in SH-SY5Y cells. Front Neurosci 13: 20, 2019.

37. Sasaki K, Hitora T, Nakamura O, Kono R and Yamamoto T: The role of MAPK pathway in bone and soft tissue tumors. Anticancer Res 31: 549-553, 2011.
38. Huang X, Zeng J, Ruan S, Lei Z, Zhang J and Cao H: The use of matrine to inhibit osteosarcoma cell proliferation via the regulation of the MAPK/ERK signaling pathway. Front Oncol 14: 1338811, 2024.
39. Ren J, Lv L, Tao X, Zhai X, Chen X, Yu H, Zhao X, Kong X, Yu Z, Dong D and Liu J: The role of CBL family ubiquitin ligases in cancer progression and therapeutic strategies. Front Pharmacol 15: 1432545, 2024.
40. Terzi EM, Sviderskiy VO, Alvarez SW, Whiten GC and Possemato R: Iron-sulfur cluster deficiency can be sensed by IRP2 and regulates iron homeostasis and sensitivity to ferroptosis independent of IRP1 and FBXL5. Sci Adv 7: eabg4302. 2021
41. Ruiz JC and Bruick RK: F-box and leucine-rich repeat protein 5 (FBXL5): Sensing intracellular iron and oxygen. J Inorg Biochem 133: 73-77, 2014.
42. Qiu C, Liu T, Luo D, Luan D, Cheng L and Wang S: Novel therapeutic savior for osteosarcoma: The endorsement of ferroptosis. Front Oncol 12: 746030, 2022.
43. Jiang M, Jike Y, Liu K, Gan F, Zhang K, Xie M, Zhang J, Chen C, Zou X, Jiang X, *et al*: Exosome-mediated miR-144-3p promotes ferroptosis to inhibit osteosarcoma proliferation, migration, and invasion through regulating ZEB1. Mol Cancer 22: 113, 2023.
44. Ma Y, Cong L, Shen W, Yang C and Ye K: Ferroptosis defense mechanisms: The future and hope for treating osteosarcoma. Cell Biochem Funct 42: e4080, 2024.
45. Nantajit D, Lin D and Li JJ: The network of epithelial-mesenchymal transition: Potential new targets for tumor resistance. J Cancer Res Clin Oncol 141: 1697-1713, 2015.
46. Cheng ZX, Wang DW, Liu T, Liu WX, Xia WB, Xu J, Zhang YH, Qu YK, Guo LQ, Ding L, *et al*: Effects of the HIF-1α and NF-κB loop on epithelial-mesenchymal transition and chemoresistance induced by hypoxia in pancreatic cancer cells. Oncol Rep 31: 1891-1898, 2014.
47. Meyers PA: Muramyl Tripeptide-Phosphatidyl ethanolamine encapsulated in liposomes (L-MTP-PE) in the treatment of osteosarcoma. Adv Exp Med Biol 1257: 133-139, 2020.
48. Traweek RS, Cope BM, Roland CL, Keung EZ, Nassif EF and Erstad DJ: Targeting the MDM2-p53 pathway in dedifferentiated liposarcoma. Front Oncol 12: 1006959, 2022.
49. Marvalim C, Datta A and Lee SC: Role of p53 in breast cancer progression: An insight into p53 targeted therapy. Theranostics 13: 1421-1442, 2023.
50. Huang R, Yang L, Zhang Z, Liu X, Fei Y, Tong WM, Niu Y and Liang Z: RNA m6A Demethylase ALKBH5 protects against pancreatic ductal adenocarcinoma via targeting regulators of iron metabolism. Front Cell Dev Biol 9: 724282, 2021.
51. Xu M, Tao J, Yang Y, Tan S, Liu H, Jiang J, Zheng F and Wu B: Ferroptosis involves in intestinal epithelial cell death in ulcerative colitis. Cell Death Dis 11: 86, 2020.
52. Geneen LJ, Dorée C and Estcourt LJ: Interventions for improving adherence to iron chelation therapy in people with sickle cell disease or thalassaemia. Cochrane Database Syst Rev 3: CD012349, 2023.
53. Sandoval-Acuña C, Torrealba N, Tomkova V, Jadhav SB, Blazkova K, Merta L, Lettlova S, Adamcová MK, Rosel D, Brábek J, *et al*: Targeting mitochondrial iron metabolism suppresses tumor growth and metastasis by inducing mitochondrial dysfunction and mitophagy. Cancer Res 81: 2289-2303, 2021.
54. Wu Y, Yu C, Luo M, Cen C, Qiu J, Zhang S and Hu K: Ferroptosis in cancer treatment: Another way to rome. Front Oncol 10: 571127, 2020.
55. Zhang B, Zhang Y, Li R, Li J, Lu X and Zhang Y: The efficacy and safety comparison of first-line chemotherapeutic agents (high-dose methotrexate, doxorubicin, cisplatin, and ifosfamide) for osteosarcoma: A network meta-analysis. J Orthop Surg Res 15: 51, 2020.
56. Wu Y, Song Y, Wang R and Wang T: Molecular mechanisms of tumor resistance to radiotherapy. Mol Cancer 22: 96, 2023.
57. Zhou J, Lan F, Liu M, Wang F, Ning X, Yang H and Sun H: Hypoxia inducible factor-1α as a potential therapeutic target for osteosarcoma metastasis. Front Pharmacol 15: 1350187, 2024.